Heat Conduction in Nanostructured Materials Predicted by Phonon Bulk Mean Free Path Distribution

Giuseppe Romano
Department of Materials Science and Engineering,
Massachusetts Institute of Technology,
77 Massachusetts Avenue,
Cambridge, MA 02139
e-mail: romanog@mit.edu

Jeffrey C. Grossman
Department of Materials Science and Engineering,
Massachusetts Institute of Technology,
77 Massachusetts Avenue,
Cambridge, MA 02139
e-mail: jcg@mit.edu

We develop a computational framework, based on the Boltzmann transport equation (BTE), with the ability to compute thermal transport in nanostructured materials of any geometry using, as the only input, the bulk cumulative thermal conductivity. The main advantage of our method is twofold. First, while the scattering times and dispersion curves are unknown for most materials, the phonon mean free path (MFP) distribution can be directly obtained by experiments. As a consequence, a wider range of materials can be simulated than with the frequency-dependent (FD) approach. Second, when the MFP distribution is available from theoretical models, our approach allows one to include easily the material dispersion in the calculations without discretizing the phonon frequencies for all polarizations thereby reducing considerably computational effort. Furthermore, after deriving the ballistic and diffusive limits of our model, we develop a multiscale method that couples phonon transport across different scales, enabling efficient simulations of materials with wide phonon MFP distributions length. After validating our model against the FD approach, we apply the method to porous silicon membranes and find good agreement with experiments on mesoscale pores. By enabling the investigation of thermal transport in unexplored nanostructured materials, our method has the potential to advance high-efficiency thermoelectric devices.
[DOI: 10.1115/1.4029775]

Keywords: heat transfer, thermoelectrics, Boltzmann transport equation

1 Introduction

Nanostructured materials have gained much attention for thermoelectric applications, thanks to their ability to effectively suppress phonon thermal conductivity (PTC) [1]. Very low thermal conductivities of thin films [2], nanowires [3], and porous materials [4–7] have recently been reported, reaching in some cases a suppression of two orders of magnitude with respect to the bulk. However, understanding these phenomena is difficult, as classical size effects become important and diffusive theories fail when the characteristic material length becomes comparable to the average phonon mean free path (MFP) [8]. Phonon classical size effects have long been modeled by means of the Casimir limit, which assumes that all phonons scatter diffusely at boundaries [9]. However, to effectively engineer thermal transport in arbitrary shapes and structures, a more accurate model of heat transport is necessary. To this end, many studies employ the BTE to compute phonon transport [10–12]. The simplest BTE model assumes that the phonon group velocities and scattering times are frequency independent, i.e., the medium is "gray." Although the gray model has been useful for understanding trends in thermal transport in many nanostructured materials, it has poor predictive power—especially for materials with wide MFP distributions. In some cases, the MFP distribution spans several orders of magnitude. For example, in Si, although the most commonly used value for the MFP is 100 nm, it has been predicted that half of the heat is carried by phonons whose MFP is greater than 1 μm [13]. Recent studies have addressed this challenge by including the full phonon distribution by successfully solving the frequency-dependent BTE (FD–BTE) for both transient and steady-state cases [14–16]. However, despite its high accuracy, the FD–BTE suffers two major limitations. First, it requires knowledge of the actual phonon dispersion curves and the phonon–phonon relaxation times, which are generally unknown for potential thermoelectric materials. The second limitation is related to computational efficiency: the FD–BTE requires the discretization of the dispersion curves and, as a result, dense sampling close to zero group velocity zones. Furthermore, as all polarizations have to be included, it becomes computationally prohibitive for materials with complex unit cells and phononic materials, where phonon dispersion curves have several branches.

In this work, we provide a new form of the steady-state BTE, with the ability to compute nanoscale heat transport using only the bulk MFP distribution as input, a quantity that can be directly obtained experimentally [17,18], while retaining the accuracy of the FD–BTE. In addition, we couple our model, which we refer to as MFP–BTE, with the ballistic BTE and the Fourier model in order to include ballistic and diffusive effects, respectively, in a consistent and seamless manner. The mapping of the bulk MFP distribution into a distribution that depends on the actual material geometry enables a deeper understanding of thermal transport in nanomaterials. We also provide a connection between the MFP-BTE and the "phonon suppression function," a useful function that describes the departure of the MFP distribution from its bulk counterpart. We apply our method to study three-dimensional classical size effects in porous Si membranes and find good agreement with experiments on mesoscale size pores. As our method can be applied to any material whose MFP distribution is known, its applicability could enable a substantially broader range of simulations of thermal transport in nanomaterials. Furthermore, in contrast to the FD–BTE approach, the MFP–BTE method is based

Contributed by the Heat Transfer Division of ASME for publication in the Journal of Heat Transfer. Manuscript received August 29, 2014; final manuscript received January 27, 2015; published online March 24, 2015. Assoc. Editor: Robert D. Tzou.

on a discretization of the MFPs, and, as such, the computational time does not increase as the number of the phonon branches increases, enabling efficient simulations of materials with complex unit cells.

2 Frequency Dependent BTE

In analogy with photon radiation, nanoscale heat transport can be described by the intensity of phonons $I(\mathbf{r},\mathbf{s},\omega,p)=v(\omega,p)\hbar\omega f(\omega,p)D(\omega,p)/(4\pi)$, where $\mathbf{r}$ is the spatial coordinate, $\mathbf{s}$ is the direction of phonon transport within a unit solid angle, ω and p are the phonon frequency and polarization, respectively, $v(\omega,p)$ is the magnitude of the phonon group velocity, $D(\omega,p)$ is the phonon density of states, $f(\omega,p)$ is the nonequilibrium phonon distribution, and $\hbar$ is the reduced Plank's constant. In its original formulation, the FD–BTE describes the intensity of phonon I under the relaxation time approximation [10]

$$\frac{1}{v}\frac{\partial I}{\partial t}+\mathbf{s}\cdot\nabla I=\frac{I^0(T_L)-I}{v\tau} \tag{1}$$

where $\tau(\omega,p)$ is the scattering time and $I^0(T_L)=v(\omega,p)\hbar\omega f^0(\omega,T_L)D(\omega,p)/(4\pi)$ is an isotropic phonon intensity parameterized by the Bose–Einstein distribution $f^0(\omega,T)=[\exp(\hbar\omega/k_BT_L)-1]^{-1}$ at a given local effective temperature $T_L(\mathbf{r})$ [19,20]. We point out that $T_L(\mathbf{r})$ is not a thermodynamic temperature but rather should be considered as a measure of the average energy of phonons at a given point. In order to compute the PTC, we apply a difference of temperature ΔT across a simulation domain with length L and calculate the thermal flux from the hot contact to the cold one. The thermal flux $\mathbf{J}(\mathbf{r})$ is computed by

$$\mathbf{J}(\mathbf{r})=4\pi\sum_p\int_0^{\omega_M^p}\langle I\mathbf{s}\rangle d\omega \tag{2}$$

where $\langle x\rangle=1/4\pi\int_{4\pi}xd\Omega$ is the angular average over the solid angle 4π, and ω_M^p is the frequency cut-off for a given polarization. In this work, we consider only the steady-state BTE, i.e., $(\partial I/\partial t)\approx 0$. The term $I^0(\mathbf{r},\mathbf{s},\omega,p)$ can be computed by applying the continuity equation to the heat flux, i.e., $\nabla\cdot\mathbf{J}(\mathbf{r})=0$ to Eq. (2), which yields

$$\sum_p\int_0^{\omega_M^p}\frac{I_0(T)}{v\tau}d\omega=\sum_p\int_0^{\omega_M^p}\frac{\langle I\rangle}{v\tau}d\omega \tag{3}$$

We note that as both $I^0(\omega,p,T)$ and $I(\omega,p)$ are frequency dependent, knowledge of the phonon dispersion curves and scattering times is required.

3 MFP Dependent BTE

In the following text, starting from Eqs. (1)–(3) we will develop a new version of the BTE where the only required input is the bulk phonon MFP distribution, given by [21]

$$K(\Lambda)=-\frac{\Lambda}{3}\sum_p C_s v\left(\frac{d\Lambda}{d\omega}\right)^{-1} \tag{4}$$

In Eq. (3), $C_s(\omega)$ is the spectral heat capacity (i.e., the volumetric heat capacity times the phonon density of states) and $\Lambda(\omega,p)=v(\omega,p)\tau(\omega,p)$ is the MFP. If the applied temperature gradient is small enough to assume that all the material properties are constant throughout the simulation domain, we can define the variable as $\tilde{T}$

$$\tilde{T}=\frac{T_{\omega,p}-T_0}{\Delta T}=4\pi\frac{I-I_0(T_0)}{C_s v\Delta T} \tag{5}$$

representing the departure from T_0 of the effective temperature $T_{\omega,p}$ associated with a given phonon frequency, polarization, and direction, normalized by ΔT. For simplicity, in our simulations we use $\Delta T=1$ and $T_0=0$. We note that a similar formulation is used in the low-variance deviational Monte Carlo approach, developed by Paraud and Hadjiconstantinou [22,23]. Including the first-order Taylor expansion [18] of $I^0(\omega,p,T_L)=I^0(\omega,p,T_0)+(1/4\pi)C_s(\omega,p)v(\omega,p)(T_L-T_0)$ in Eq. (3), we have

$$\Lambda\mathbf{s}\cdot\nabla[I-I^0(T_0)]+I-I^0(T_0)=C_s v\left[\sum_p\int_0^{\omega_p'}\frac{C_s}{\tau}d\omega'\right]^{-1}\sum_{p'}\int_0^{\omega_M^{p'}}\frac{\langle I-I^0(T_0)\rangle}{\Lambda}d\omega' \tag{6}$$

where we use the fact that $I^0(T_0)$ is isotropic and spatially independent. We note that Eq. (6) still needs the phonon scattering times and dispersion curves. If we use the new variable $\tilde{T}$, named "mode temperature," Eq. (6) can be rearranged into

$$\Lambda\mathbf{s}\cdot\nabla\tilde{T}+\tilde{T}=\gamma\int_0^\infty\frac{K}{\Lambda^2}\langle\tilde{T}\rangle d\Lambda' \tag{7}$$

where $\gamma=\left[\int_0^\infty\left(K/\Lambda^2\right)d\Lambda\right]^{-1}$ is a material property, which for Si is $\gamma_{Si}=2.2739\times10^{-17}\mathrm{m^3W^{-1}K}$. Note that the right-hand side of Eq. (7) is equal to $\tilde{T}_L(\mathbf{r})=((T_L(\mathbf{r})-T_0)/\Delta T)$, which is the normalized local temperature. Since Eq. (7) requires only the bulk MFP distribution as input, we will refer to it as the MFP dependent BTE or *MFP–BTE* for short. We note that in deriving Eq. (7), we have assumed isotropic BZ. Further studies will be devoted to including anisotropicity in the MFP-BTE.

4 Boundary Conditions

According to Refs. [15,24], for the FD–BTE, periodic boundary conditions have to be applied to the departure of the phonon intensity from equilibrium. For example, if $\mathbf{P}$ is the periodicity vector, we have

$$I(\mathbf{r}+\mathbf{P},\mathbf{s},\omega,p)-I_0(\mathbf{r}+\mathbf{P},\omega)=I(\mathbf{r},\mathbf{s},\omega,p)-I_0(\mathbf{r},\omega) \tag{8}$$

It is possible to show that, in the case of MFP–BTE, we simply need to apply $\Delta\tilde{T}=1$. Partially diffusive boundary conditions on a surface, with normal $\mathbf{n}$, can be applied by imposing

$$\tilde{T}(\mathbf{r},\mathbf{s})=(1-p)\frac{1}{\pi}\int_{\mathbf{s}'\cdot\mathbf{n}>0}\tilde{T}(\mathbf{r},\mathbf{s}')\mathbf{s}'\cdot\mathbf{n}d\Omega+p\tilde{T}(\mathbf{r},\mathbf{s_i}) \tag{9}$$

where $\mathbf{s_i}=\mathbf{s}-2|\mathbf{s}\cdot\mathbf{n}|\mathbf{n}$ is the specular direction related to the surface with normal $\mathbf{n}$, and p is the specularity parameter, depending on surface roughness [19]. Finally, a prescribed temperature T_p can be enforced by simply imposing $\tilde{T}=T_p$.

5 Effective Thermal Conductivity

Within the MFP–BTE formulation, the thermal flux can be obtained by $\mathbf{J}=3\Delta T\int_0^\infty(K(\Lambda)/\Lambda)\langle\tilde{T}(\Lambda)\rangle\mathbf{s}d\Lambda$. Once Eq. (7) converges, we can compute the PTC by combining Eq. (2) with Fourier's Law

$$\kappa_{\mathrm{eff}}=\frac{3L}{A}\int_\Gamma\int_0^\infty\frac{K}{\Lambda}\langle\tilde{T}\mathbf{s}\cdot\mathbf{n}\rangle d\Lambda dS \tag{10}$$

where Γ is either the cold or hot contact, and A is its area. In Eq. (10), we use $\langle I^0\mathbf{s}\rangle=0$, because I^0 is isotropic. We note that Eqs. (7)–(10) do not require the use of ΔT. It is useful at this point to define the phonon suppression function

$$S(\Lambda)=\frac{3L}{\Lambda A}\int_\Gamma\langle\tilde{T}\mathbf{s}\cdot\mathbf{n}\rangle dS \tag{11}$$

which yields a simpler formula for the PTC $\kappa_{\text{eff}} = \int_0^\infty K(\Lambda)S(\Lambda)d\Lambda$. If we denote the MFP distribution in the nanostructured material as $K^{\text{nano}}(\Lambda)$, the phonon suppression function can be formally defined by $S(\Lambda) = K^{\text{nano}}(\Lambda)/K(\Lambda)$. Although defined differently, $S(\Lambda)$ is essentially the same as the material independent *boundary function* $D(\Lambda^{\text{nano}}/\Lambda) = \Lambda^{\text{nano}}/\Lambda$ introduced by Yang and Dames in Ref. [21], where Λ_{nano} is the MFP in the nanostructured material, except that within our formalism $S(\Lambda)$ may in general depend on the material. We note that the physical meaning of $S(\Lambda)$ is slightly different from the phonon suppression function defined in recently developed MFP distribution measurement techniques [17,18], where the suppression function refers to the suppression of heat flux due to the finite thermal length induced in the bulk material.

6 Ballistic Limit of the MFP–BTE

In order to derive the ballistic limit of the MFP–BTE, we define the Knudsen number as $\text{Kn} = \Lambda/L$. For nanostructures with $\text{Kn} \gg 1$, phonons travel primarily ballistically and their effective MFPs approach the characteristic length of the material. Within this regime, it is possible to show that the mode temperature distributions are MFP independent. Under this simplification, Eq. (7) turns into

$$\Lambda \mathbf{s} \cdot \nabla \tilde{T} + \tilde{T} = \text{const} \tag{12}$$

which is the ballistic BTE [25]. Equation (12) is computationally less expensive than the MFP–BTE because phonons with different MFPs are decoupled from each other.

7 Diffusive Limit of the MFP–BTE

Following a similar approach as in Ref. [16], the diffusive limit of the MFP–BTE can be obtained by using the first spherical expansion of $\tilde{S}(\mathbf{r},\mathbf{s})$. Given a small perturbation, $\Phi(\mathbf{r}) \cdot \mathbf{s}$ in the $\mathbf{s}$ direction, the inclusion of the spherical expansion of $\tilde{T}(\mathbf{r},\mathbf{s}) = \langle \tilde{T}(\mathbf{r},\mathbf{s}) \rangle + \Phi(\mathbf{r}) \cdot \mathbf{s}$ into Eq. (7) leads to

$$\tilde{T} = \gamma \int_0^\infty \frac{K}{\Lambda'^2} \langle \tilde{T} \rangle d\Lambda' - \Lambda \nabla \cdot \langle \mathbf{s}\tilde{T} \rangle \tag{13}$$

where $\nabla \cdot \phi \ll \Lambda \nabla \cdot \langle \mathbf{s}\tilde{T} \rangle$ is used. The corresponding heat flux, $\mathbf{J} = -K3\Delta T \nabla \langle \tilde{T} \rangle$, which is obtained by multiplying both sides of Eq. (13) by $(3\Delta TK/\Lambda)\mathbf{s}$ and integrating them over the solid angle, is now diffusive. The continuity equation for the thermal flux, derived by multiplying by $3\Delta TK/\Lambda$ both sides of Eq. (7) and computing an angular average, is given by

$$\nabla \cdot \mathbf{J} = \frac{3\Delta TK}{\Lambda^2} \left(\gamma \int_0^\infty \frac{K}{\Lambda'^2} \langle \tilde{T} \rangle d\Lambda' - \langle \tilde{T} \rangle \right) \tag{14}$$

The combination of Eqs. (14) and (13) leads to

$$\Lambda^2 \nabla^2 \langle \tilde{T} \rangle - \langle \tilde{T} \rangle = \gamma \int_0^\infty \frac{K}{\Lambda'^2} \langle \tilde{T} \rangle d\Lambda' \tag{15}$$

which is a diffusive equation with the right-hand side acting as an effective heat source and describing the energy balance among different phonon modes. We refer to Eq. (15) as the modified Fourier equation (MFE) [16].

8 Fourier/BTE Coupling

The solution of Eq. (7) requires the discretization of the simulation domain into a mesh whose characteristic size should be at least as small as the smallest MFP, making the phonon transport calculation in materials with wide MFP distributions computationally expensive. To solve this numerical issue, we define a threshold in the Knudsen number Kn_D, below which phonons are solved by means of the MFE. Being defined directly in term of $\langle \tilde{T} \rangle$, Eq. (15) is computationally less intensive than the MFP–BTE, but at the expense of neglecting scattering between phonons and material boundaries [16]. We also identify a threshold Kn_B, above which all phonons are solved by means of Eq. (12). As in the ballistic regime, all phonon modes are decoupled from each other, and Eq. (12) has to be solved only once. By solving iteratively Eqs. (7), (12), and (15), we ensure energy conservation among all phonon modes, which are linked to each other through $T_{\text{L}}(\mathbf{r})$. The first guess for $T_{\text{L}}(\mathbf{r})$ is given by Fourier's simulation [26]. A general approach for choosing the transition points among different regimes is to start with the reasonable guess $\text{Kn}_D = \text{Kn}_B = 1$. Then, we push Kn_D and Kn_B toward lower and higher values, respectively, until convergence in the heat flux is reached.

9 Discretization Details

The solution of the MFP–BTE requires the discretization of the solid angle. Here, we use simple uniform sampling, although a more sophisticated technique, i.e., based on Gaussian integration, would enable the use of coarser grids [16]. The solid angle is discretized into N_θ azimuthal and N_ϕ polar angles. The center direction for each slice is

$$\mathbf{s}_{kl} = \sin(\theta_k)\sin(\phi_l)\hat{\mathbf{x}} + \sin(\theta_k)\cos(\phi_l)\hat{\mathbf{y}} + \cos(\theta_k)\hat{\mathbf{z}} \tag{16}$$

where $k = 0...N_\theta, l = 0...N_\phi$. After integrating Eq. (7) over the control angle denoted by the indexes kl, we have

$$\frac{\Lambda}{\Delta\Omega_{kl}} \mathbf{S}_{kl} \cdot \nabla \tilde{T} + \tilde{T} = \gamma \int_0^\infty \frac{K}{\Lambda'^2} \langle \tilde{T} \rangle d\Lambda' \tag{17}$$

where $\mathbf{S}_{kl}$ is given by

$$\begin{aligned} \mathbf{S}_{kl} &= \sin(\phi_l)\sin(0.5\Delta\phi_l)[\Delta\theta_k - \cos(2\theta)\sin(\Delta\theta_k)]\hat{\mathbf{x}} \\ &= \cos(\phi_l)\sin(0.5\Delta\phi_l)[\Delta\theta_k - \cos(2\theta)\sin(\Delta\theta_k)]\hat{\mathbf{y}} \\ &= 0.5\Delta\phi_l \sin(2\theta_k)\sin(\Delta\theta_k)\hat{\mathbf{z}} \end{aligned} \tag{18}$$

and $\Delta\Omega_{kl} = 2.0\sin(\theta_k)\sin(0.5\Delta\theta_k)\Delta\phi_l$. In Eq. (18), $\Delta\theta_k$ and $\Delta\phi_l$ refer to the discretization of the angle θ_k and ϕ_l, respectively. The MFP–BTE requires the iterative solution of Eq. (17). The MFP–BTE is computed N times, where N is the number of MFPs used to span the whole range of the bulk phonon MFP distribution. The resulting set of MFPs is $\Lambda_n = \Lambda_1...\Lambda_N$ and is logarithmically equally spaced. Once the distributions for $\tilde{T}(\Lambda_m)$ are obtained, we calculate the new lattice temperature by the integral appearing at the right-hand side of Eq. (17). This integration has to be carried out carefully, as for computational reasons N is typically smaller than the number of MFPs M needed for an accurate description of $K(\Lambda)$. To facilitate the following analysis, we define a new set of MFPs $\tilde{\Lambda}_k = \tilde{\Lambda}_1...\tilde{\Lambda}_M$ and the associated sampling of the MFP distribution $K_k = K(\tilde{\Lambda}_k)$. The calculation of the lattice temperature requires the mapping $\Lambda \to \tilde{\Lambda}$. To this end, a simple linear interpolation leads to $\tilde{T}_k = \tilde{T}(\Lambda_{n_k})(1 - g_k) + \tilde{T}(\Lambda_{n_k+1})g_k$, where $g_k = ((\Lambda_{n_k+1} - \tilde{\Lambda}_k)/(\Lambda_{n_k+1} - \Lambda_n))$ and n_k is the largest n such that $\Lambda_n < \tilde{\Lambda}_k$. According to this notation, the normalized lattice temperature can be computed as

$$\tilde{T}_L = \gamma \sum_k \frac{K_k}{\Lambda_k^2} \left[\langle \tilde{T}(\Lambda_{n_k}) \rangle (1 - g_k) + \langle \tilde{T}(\Lambda_{n_k+1}) \rangle g_k \right] \Delta\Lambda_k \tag{19}$$

The solution of the MFP–BTE for a given Λ_n is given below in a more concise form

$$\frac{\Lambda_n}{\Delta\Omega_{kl}} \mathbf{S}_{kl} \cdot \nabla \tilde{T} + \tilde{T} = \tilde{T}_{\text{L}} \tag{20}$$

which has to be discretized spatially, as well. We used the finite volume (FV) method, which determines the mode temperature at the center of each cell. The FV discretization of the MFP–BTE can be obtained by integrating Eq. (20) over the control volume ΔV_m

$$\frac{\Lambda_n}{\Delta\Omega_{kl}}\int_{\Delta V_m}\mathbf{S}_{kl}\cdot\nabla\tilde{T}dV+\int_{\Delta V_m}\tilde{T}dV=\int_{\Delta V_m}\tilde{T}_{\mathrm{L}}dV \tag{21}$$

In the FV approach, the temperature within each cell is considered constant throughout the cell, hence Eq. (21) becomes

$$\frac{\Lambda_n}{\Delta V_m\Delta\Omega_{kl}}\int_{\Delta S}\tilde{T}\mathbf{S}_{kl}\cdot\mathbf{n}dS+\tilde{T}=\tilde{T}_{\mathrm{L}} \tag{22}$$

where we used Gauss's theorem. In Eq. (22), **n** is the normal to the surface along which the integration is carried out. The actual implementation of Eq. (22) may follow different approaches. In our case, we use the upwind scheme, which is described in the following. According to Fig. 1(*c*), let the centroid of an arbitrary cell be **P**, whereas a point belonging to one of its sides, with normal **n**, is denoted by **B**. According to the upwind scheme, $\tilde{T}(\mathbf{B})=\tilde{T}(\mathbf{P})$ only if $\mathbf{n}\cdot\mathbf{s}>0$. Further details regarding the implementation of the upwind FV method for the BTE can be found in Refs. [16,26].

10 Two-Dimensional Simulations

In order to assess the accuracy of our model, we compare the MFP–BTE with the FD–BTE for two-dimensional porous Si. Then, we ensure that the diffusive limit is fully recovered by comparing analytical data with results obtained with a macroscale domain.

10.1 MFP/FD–BTE Comparison. The FD–BTE requires as input the phonon dispersions and scattering times. Specifically for the FD–BTE/MFP–BTE comparison, i.e., we use $p=0$ in Eq. (9) and only the dispersion curves along *100* are considered [14]. The phonon frequencies, shown in Fig. 2(*a*), are computed by means of first principles calculations by using the QUANTUM ESPRESSO software package [27]. The Umklapp and isotopic phonon scattering times are obtained by

$$1/\tau_u=A\omega^2T\exp(B/T) \tag{23}$$

$$1/\tau_i=C\omega^4 \tag{24}$$

where A, B, and C are parameters used to fit experimental data for bulk Si [14]. The total scattering time is simply obtained by using

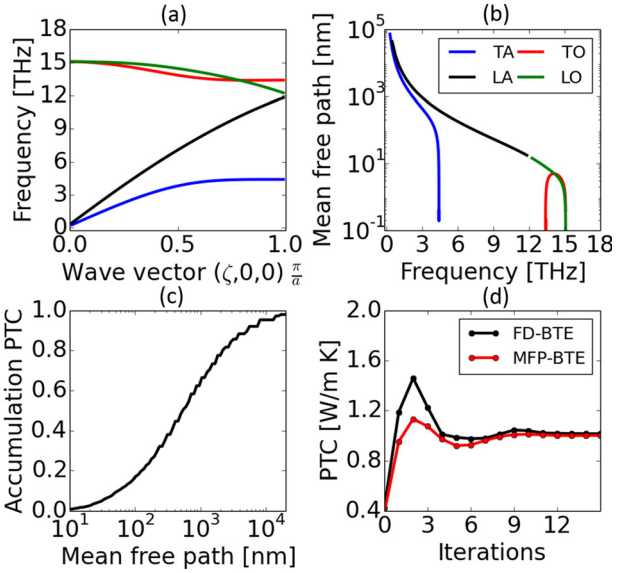

Fig. 2 (*a*) Phonon dispersion along the 001 direction computed by first-principles calculations, (*b*) the MFPs for different phonon polarizations, (*c*) the cumulative thermal conductivity at room temperature, and (*d*) comparison between the FD–BTE and the MFP–BTE method for a unit cell of size $L=10$ nm. After a few iterations, the two methods lead to the same thermal conductivity.

Matthiessen's rule $1/\tau=1/\tau_u+1/\tau_i$. The phonon MFPs for each polarization are shown in Fig. 2(*b*) whereas the accumulation PTC used for the MFP–BTE is reported in Fig. 2(*c*). We consider a unit cell with length $L=10$ nm containing one pore with diffusive walls. Periodic boundary conditions along the heat flux direction are applied and a fixed porosity $\phi=0.25$ is considered. According to Fig. 2(*d*), the MFP–BTE produces the same results as the FD–BTE, demonstrating the equivalence between the two methods. We note that for the MFP–BTE we have to discretize only one function, i.e., the bulk MFP distribution, whereas the FD–BTE requires the discretization of the phonon dispersion curves for each polarization, increasing the computational effort—especially for complex unit cell materials, such as Bi_2Te_3. The computational efficiency of the MFP–BTE can be further increased if we use a power law interpolation. In fact, $\tilde{S}(\Lambda)$ is typically a smooth function in Λ, and goes as $1/\Lambda$ toward the ballistic limit. For the FD–BTE, however, the phonon dispersion curves

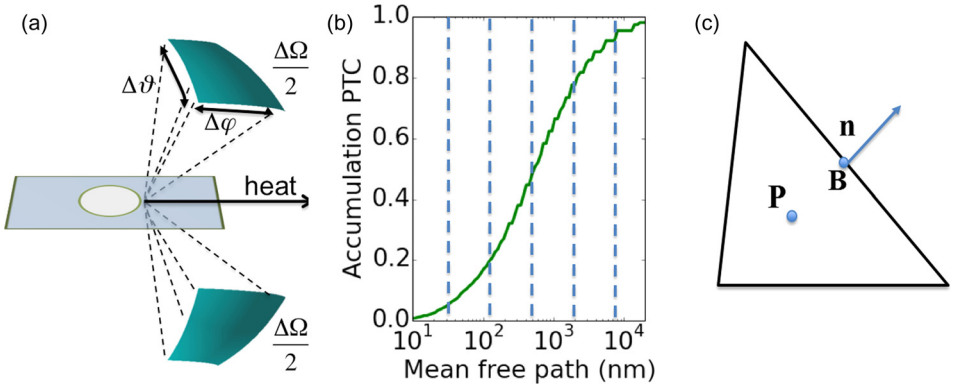

Fig. 1 (*a*) Discretization of the solid angle in slices of $\Delta\Omega$. Because the system is two-dimensional, we consider only the upper hemisphere and then apply the symmetry. (*b*) The cumulative thermal conductivity of Si, the only input required by the MFP–BTE. The MFP range is discretized into a small number of MFPs, typically a few tenths, for which the MFP–BTE is solved. (*c*) An example of a triangular element of the simulation domain. The centroid is denoted by P, whereas the point at the middle of the side with normal n is denoted by B.

may require a dense interpolation in those zones with small group velocity [14].

10.2 Phonon Suppression Function. We now analyze the phonon suppression function, as given in Eq. (11), for a porous material with circular pores and a periodicity of $L = 100$ nm. According to Fig. 3(*a*), for very small MFPs, $S(\Lambda)$ reaches its maximum value and does not depend on the MFP any longer. That is, we are approaching the diffusive regime. For very large MFPs, the suppression function decreases abruptly and goes as $1/\Lambda$, the typical trend for the ballistic regime. The transition point can be exploited by looking at the derivative of $S(\Lambda)$ with respect to the MFP, shown in Fig. 3(*b*). The maximum of the $|S'(\Lambda)|$, that is the MFP above which the suppression functions is about 0.5, is around 44 nm, which is the pore–pore distance. The suppression function can hence provide a useful way to identify the characteristic length of a nanomaterial, which is the MFP that leads to $S''(\Lambda) = 0$. Further studies may be devoted to exploring whether or not it is possible to have multiple characteristic lengths. The introduction of $S'(\Lambda)$ leads to an alternative formula for the reduction of the PTC due to size effects

$$r(\Lambda) = \frac{\kappa_{\text{eff}(\Lambda)}}{\kappa_{\text{bulk}}} = -\int_0^{\infty} S'(\Lambda)\alpha(\Lambda)d\Lambda \tag{25}$$

where $\alpha(\Lambda) = 1/\kappa_{\text{bulk}} \int_0^{\Lambda} K(\Lambda')d\Lambda'$ is the normalized cumulative thermal conductivity, a function defining the total amount of heat carried by phonons whose MFP is below Λ [28]. In Eq. (25), we used $S(\infty) = 0$ and $\alpha(0) = 0$ [21]. From Fig. 3(*b*), it is clear that low thermal conductivities can be obtained by (i) having characteristic lengths equal to MFPs for which $\alpha(\Lambda)$ is relatively low and (ii) having narrow $S'(\Lambda)$. While this work is based primarily on methodology, optimizing material geometry to meet these conditions is beyond the scope of our study.

10.3 Diffusive Limit. We now further validate our code by allowing the length of the unit cell to reach macroscopic scales. In Fig. 4(*a*), the effective temperature computed by the MFP–BTE for the $L = 100$ nm case is reported. As we can see from Fig. 4(*b*), phonons mostly travel in the spaces between pores, due to collisions with pore boundaries

In Fig. 4(*c*), the cumulative thermal conductivity $a^{\text{nano}}(\Lambda) = \kappa_{\text{bulk}} \int_0^{\Lambda} K(\Lambda')S(\Lambda')d\Lambda'$ is plotted for different length scales. According to Fig. 4(*c*), for $L = 10$ nm, the PTC is $\kappa_{\text{eff}} = 5$ W/mK while for very large pores the thermal transport reaches the diffusive limit, as predicted by Hashin and Shtrikman [29] $\kappa_{\text{eff}}/\kappa_{\text{bulk}} = (1-\phi)/(1+\phi) \approx 89.5$ W/mK. The optimum values for the transition Knudsen numbers are $\text{Kn}_D = 0.1$ and $\text{Kn}_B = 10$. We have also performed calculations without using the multiscale scheme described above and similar results have been obtained.

11 Three-Dimensional Simulations

In order to simulate realistic, three-dimensional systems, we use the bulk MFP distribution computed by first principles [30]. In the Secs. 11.1 and 11.2, we consider both nanoscale and mesoscale structures, respectively.

11.1 Silicon Nanomesh. We calculate the thermal flux across the Si nanomesh studied in Ref. [5] with length $L = 34$ nm, porosity $\phi = 0.173$, and height $H = 22$ nm. In Fig. 5(*a*), we plot the cumulative thermal conductivity. The measured value is about only $\kappa_{\text{eff}} = 2.85$ W/mK [5], while the computed PTC is 8 W/m K. Aside from unavoidable errors in measuring thermal conductivities at the nanoscale, this discrepancy could suggest the presence of phonon wave effects. However, according to Ref. [31], such a low experimental PTC can be justified by the presence of an amorphous layer along the pore walls, leading to a higher effective porosity. We remark here that our work neglects wave effects, hence the reduction of the PTC arises only from the scattering between phonons and the boundaries. Phonon wave effects may dominate thermal transport at room temperature in certain systems such as those composed of thin films with periodic nanopillars [32], where local resonances cause band flattening. Such effects and wave effects in general are beyond the scope of this study.

11.2 Porous-Silicon Membrane. We now consider a mesoscale porous Si membrane with $L = 4$ μm and height $H = 4.49$ μm, as reported experimentally in Ref. [4]. As shown in Fig. 5(*b*), heat travels primarily in the spaces between pores along the direction of the imposed temperature gradient. The top and bottom surfaces are considered purely diffusive and act as additional scattering sources. This effect can be further understood if we examine the cut in the magnitude of thermal flux reported in Fig. 5(*c*). In fact, most of the thermal flux is concentrated in the middle of the

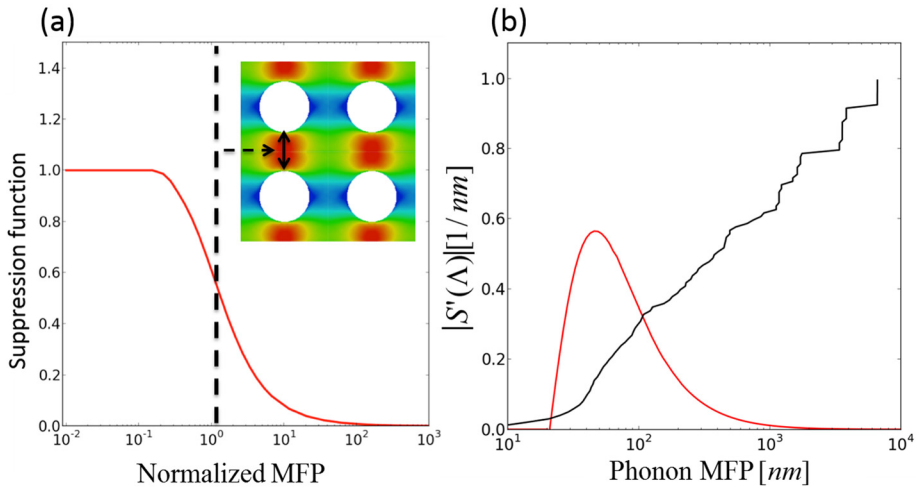

Fig. 3 (*a*) The phonon suppression function $S(\Lambda)$, normalized to 1. For very small MFPs, $\tilde{S}$ reaches its maximum values and becomes flat, meaning that we are reaching the diffusive regime. For very large MFPs, the suppression function goes into the ballistic regime, namely, $S \approx 1/\Lambda$. In the inset, the magnitude of the thermal flux is shown. (*b*) The derivative of the suppression function $|S'(\Lambda)|$ superimposed on the cumulative thermal conductivity of Si. The maximum of $|S'(\Lambda)|$ is obtained for a MFP that equals the pore–pore distance.

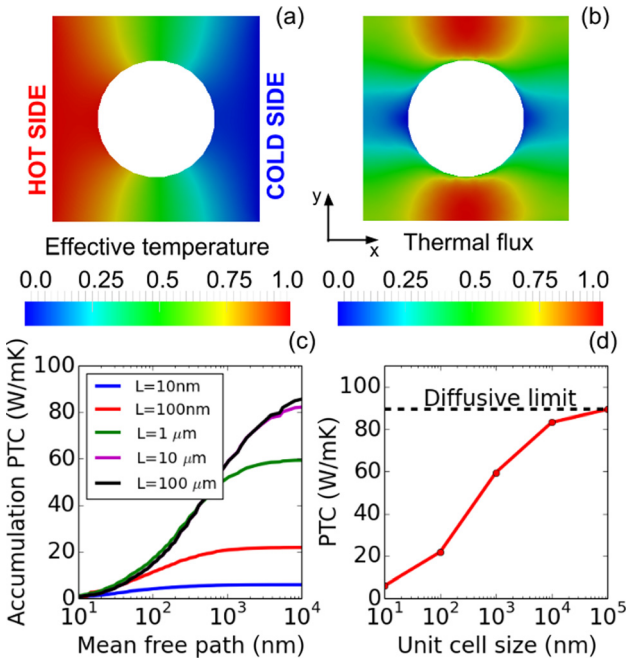

Fig. 4 (*a*) Effective temperature map for the $L = 100$ nm case. The normalized heat flux is ensured by applying a difference of temperature to the unit cell. (*b*) Normalized magnitude of thermal flux. Most of the heat travels in the space between pores. (*c*) Cumulative for different sizes of the unit cell L, ranging from the nanoscale to the macroscale. (*d*) PTC versus the unit cell size. For macroscales, the effective thermal conductivity reaches the diffusive regime.

sample, leading to further reduction in the PTC. As the scattering with the top and bottom surfaces is not included in the MFE, the optimum threshold in the Knudsen number is lower than the one used for the 2D case and is determined to be $K_D = 0.025$. The computed PTC is about $\kappa_{\text{eff}} = 56$ W/mK, while the experimental value is 45 W/m K. Considering the error in the measurements for

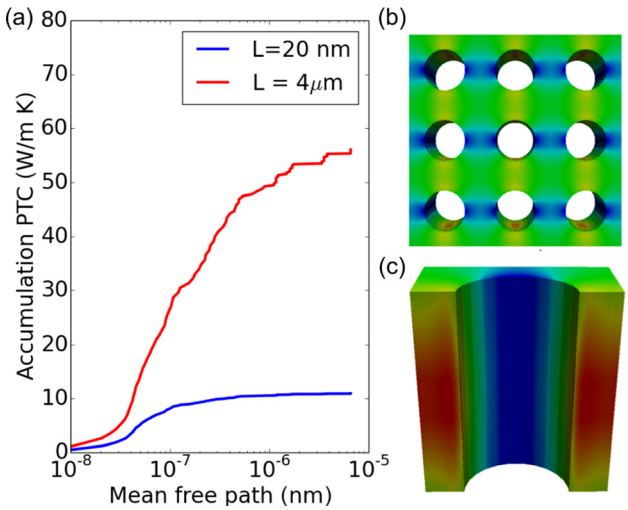

Fig. 5 (*a*) The cumulative thermal conductivity for a mesoscale porous-Si membrane [4] and Si nanomesh [5]. Phonon classical size effects strongly depend on the limiting dimension that is the smallest between the pore size and the sample thickness. (*b*) The magnitude of the thermal flux for the periodic structure. Phonons travel between pores along the direction of the gradient of the temperature, due to phonon-pore scattering. (*c*) A cut of magnitude of the thermal flux map. Most of the heat is concentrated toward the middle of the sample due to the diffuse scattering of phonons with the top and bottom surfaces.

thin films [32], the two results are in good agreement with each other. We note that the best numerical estimation to date is 67 W/m K, obtained by the MFP sampling method [32]. We remark that, although the simulation domain is in the mesoscale regime, the above results have been obtained with no input parameters, demonstrating the validity of our multiscale method. We remark that while the method has been applied to Si, its validity is general and any material can be modeled, as long as its bulk MFP distribution is known, either experimentally or computed by first principles.

12 Conclusions

In summary, we have developed an efficient method based on the BTE with the ability to compute the PTC without requiring prior knowledge of the phonon dispersion curve and three-phonon scattering times, using only the bulk MFP distribution as input, which can be directly obtained through experiments. In addition to its wide range of applicability, this method is more computationally efficient than the FD–BTE, particularly for materials with complex unit cells. Our results show good agreement with measurements on mesoscale porous Si membranes, showing the validity of the model across different length scales.

Acknowledgment

We thank Keivan Esfarjani and Gang Chen for providing the phonon mean free path distribution of Si computed by first principles. We thank Yongjie Yu, Aldo Di Carlo, and Alexie Kolpak for useful discussions.

Nomenclature

A = area of the contact (m^2)
$\mathbf{B}$ = point along a element's boundary (m)
C_s = spectral-volumetric heat capacity (J m^{-3} K^{-1} s)
D = density of states (m^{-3}s)
f = distribution function
g = interpolation function
$\hbar$ = reduced Plank's constant (J s)
I = phonon intensity ($Wm^{-2}sr^{-1}s$)
I^0 = equilibrium phonon intensity ($Wm^{-2}sr^{-1}s$)
K = MFP distribution in bulk (W m^{-2} K^{-1})
K^{nano} = MFP distribution in the nanosystem (W m^{-2} K^{-1})
Kn = Knudsen number
L = distance between the hot and cold contact (m)
$\mathbf{n}$ = normal vector
N_θ = number of azimuthal angles
N_ϕ = number of polar angles
$\mathbf{P}$ = element's centroid (m)
$\mathbf{r}$ = position vector (m)
$\mathbf{s}$ = phonon direction
$\mathbf{S}$ = integrated phonon direction (sr)
S = suppression function
T_L = lattice temperature
$\tilde{T}$ = normalized mode temperature
$\tilde{T}_L$ = normalized lattice temperature
$T_{\omega,p}$ = mode temperature (K)
T_0 = equilibrium temperature (K)
v = group velocity (ms^{-1})
α = cumulative thermal conductivity in bulk
γ = material property (K W^{-1} m^{-3})
ΔT = applied difference of temperature (K)
$\Delta\omega$ = solid angle discretization (sr)
Λ = MFP in bulk (m)
Λ^{nano} = MFP in the nanosystem (m)
$\tilde{\Lambda}$ = MFP discretization (m)
κ_B = Boltzmann's constant (J K^{-1})
κ_{bulk} = bulk thermal conductivity ($Wm^{-1}K^{-1}$)
κ_{eff} = effective thermal conductivity (W m^{-1} K^{-1})

τ = relaxation time (s)
ϕ = material's porosity
Φ = small perturbation to the mode temperature
Ω = solid angle (sr)
ω = angular frequency of phonons (rad s^{-1})
ω_M^p = maximum angular frequency for a given polarization p (rad s^{-1})

References

[1] Majumdar, A., 2004, "Thermoelectricity in Semiconductor Nanostructures," Science, **303**(5659), pp. 777–778.
[2] Venkatasubramanian, R., Siivola, E., Colpitts, T., and O' Quinn, B., 2001, "Thin-Film Thermoelectric Devices With High Room-Temperature Figures of Merit," Nature, **413**(6856), pp. 597–602.
[3] Hochbaum, A. I., Chen, R., Delgado, R. D., Liang, W., Garnett, E. C., Najarian, M., Majumdar, A., and Yang, P., 2008, "Enhanced Thermoelectric Performance of Rough Silicon Nanowires," Nature, **451**(7175), pp. 163–167.
[4] Song, D., and Chen, G., 2004, "Thermal Conductivity of Periodic Microporous Silicon Films," Appl. Phys. Lett., **84**(5), pp. 687–689.
[5] Yu, J.-K., Mitrovic, S., Tham, D., Varghese, J., and Heath, J. R., 2010, "Reduction of Thermal Conductivity in Phononic Nanomesh Structures," Nat. Nanotechnol., **5**(10), pp. 718–721.
[6] Tang, J., Wang, H.-T., Lee, D. H., Fardy, M., Huo, Z., Russell, T. P., and Yang, P., 2010, "Holey Silicon as an Efficient Thermoelectric Material," Nano Lett., **10**(10), pp. 4279–4283.
[7] Lee, J.-H., Galli, G. A., and Grossman, J. C., 2008, "Nano Si as an Efficient Thermoelectric Material," Nano Lett., **8**(11), pp. 3750–3754.
[8] Chen, G., 2005, *Nanoscale Energy Transport and Conversion: A Parallel Treatment of Electrons, Molecules, Phonons, and Photons*, Oxford University Press, New York.
[9] Casimir, H., 1938, "Note on the Conduction of Heat in Crystals," Physica, **5**(6), pp. 495–500.
[10] Majumdar, A., 1993, "Microscale Heat Conduction in Dielectric Thin Films," ASME J. Heat Transfer, **115**(1), pp. 7–16.
[11] Chen, G., 1998, "Thermal Conductivity and Ballistic-Phonon Transport in the Cross-Plane Direction of Superlattices," Phys. Rev. B, **57**(3), pp. 14958–14973.
[12] Cahill, D. G., Ford, W. K., Goodson, K. E., Mahan, G. D., Majumdar, A., Maris, H. J., Merlin, R., and Phillpot, S. R., 2003, "Nanoscale Thermal Transport," J. Appl. Phys., **93**(2), pp. 793–818.
[13] Esfarjani, K., Chen, G., and Stokes, H. T., 2011, "Heat Transport in Silicon From First-Principles Calculations," Phys. Rev. B, **84**(8), p. 085204.
[14] Minnich, A. J., Chen, G., Mansoor, S., and Yilbas, B. S., 2011, "Quasiballistic Heat Transfer Studied Using the Frequency-Dependent Boltzmann Transport Equation," Phys. Rev. B, **84**(23), p. 235207.
[15] Hsieh, T.-Y., Lin, H., Hsieh, T.-J., and Huang, J.-C., 2012, "Thermal Conductivity Modeling of Periodic Silicon With Aligned Cylindrical Pores," J. Appl. Phys., **111**(12), p. 124329.
[16] Loy, J. M., Murthy, J. Y., and Singh, D., 2013, "A Fast Hybrid Fourier–Boltzmann Transport Equation Solver for Nongray Phonon Transport," ASME J. Heat Transfer, **135**(1), p. 011008.
[17] Minnich, A. J., Johnson, J., Schmidt, A., Esfarjani, K., Dresselhaus, M., Nelson, K. A., and Chen, G., 2011, "Thermal Conductivity Spectroscopy Technique to Measure Phonon Mean Free Paths," Phys. Rev. Lett., **107**(9), p. 095901.
[18] Minnich, A. J., 2012, "Determining Phonon Mean Free Paths From Observations of Quasiballistic Thermal Transport," Phys. Rev. Lett., **109**(20), p. 205901.
[19] Ziman, J. M., 2001, *Electrons and Phonons: The Theory of Transport Phenomena in Solids*, OUP, Oxford, UK.
[20] Mingo, N., Stewart, D., Broido, D., Lindsay, L., and Li, W., 2014, "Ab Initio Thermal Transport," *Length-Scale Dependent Phonon Interactions*, Springer, Berlin, pp. 137–173.
[21] Yang, F., and Dames, C., 2013, "Mean Free Path Spectra as a Tool to Understand Thermal Conductivity in Bulk and Nanostructures," Phys. Rev. B, **87**(3), p. 035437.
[22] Paraud, J. P. M., and Hadjiconstantinou, N. G., 2011, "Efficient Simulation of Multidimensional Phonon Transport Using Energy-Based Variance-Reduced Monte Carlo Formulations," Phys. Rev. B, **84**(20), p. 205331.
[23] Paraud, J. P. M., and Hadjiconstantinou, N. G., 2012, "An Alternative Approach to Efficient Simulation of Micro/Nanoscale Phonon Transport," Appl. Phys. Lett., **101**(15), p. 153114.
[24] Jeng, M.-S., Yang, R., Song, D., and Chen, G., 2008, "Modeling the Thermal Conductivity and Phonon Transport in Nanoparticle Composites Using Monte Carlo Simulation," ASME J. Heat Transfer, **130**(4), p. 042410.
[25] Chen, G., 2001, "Ballistic-Diffusive Heat-Conduction Equations," Phys. Rev. Lett., **86**(11), pp. 2297–2300.
[26] Romano, G., and Di Carlo, A., 2011, "Multiscale Electrothermal Modeling of Nanostructured Devices," IEEE Trans. Nanotechnol., **10**(6), pp. 1285–1292.
[27] Giannozzi, P., Baroni, S., Bonini, N., Calandra, M., Car, R., Cavazzoni, C., Ceresoli, D., Chiarotti, G. L., Cococcioni, M., Dabo, I., Dal Corso, A., De Gironcoli1, S., Fabrisi, S., Fratesi, G., Gebauer, R., Gerstmann, U., Gougoussis, C., Kokalj, A., Lazzeri, M., Martin-Samos, L., Marzari, N., Mauri, F., Mazzarello, R., Paolini, S., Pasquarello, A., Paulatto, L., Sbraccia, C., Scandolo, S., Sclauzero, G., Seitsonen, A. P., Smogunov, A., Umari, P., and Wentzcovitch, R. M., 2009, "QUANTUM ESPRESSO: A Modular and Open-Source Software Project for Quantum Simulations of Materials," J. Phys.: Condens. Matter, **21**(39), p. 395502.
[28] Slack, G. A., 1994, *Handbook of Thermoelectrics*, D. M. Rowe, ed., CRC Press, Boca Raton, FL, p. 407.
[29] Hashin, Z., and Shtrikman, S., 1962, "A Variational Approach to the Theory of the Effective Magnetic Permeability of Multiphase Materials," J. Appl. Phys., **33**(10), pp. 3125–3131.
[30] Esfarjani, K., Chen, G., and Stokes, H. T., 2011, "Heat Transport in Silicon From First-Principles Calculations," Phys. Rev. B, **84**(8), p. 085204.
[31] Ravichandran, N. K., and Minnich, A. J., 2014, "Coherent and Incoherent Thermal Transport in Nanomeshes," Phys. Rev. B, **89**, p. 205432.
[32] Davis, B. L., and Hussein, M. I., 2014, "Nanophononic Metamaterial: Thermal Conductivity Reduction by Local Resonance," Phys. Rev. Lett., **112**, p. 055505.
[33] Jain, A., Yu, Y.-J., and McGaughey, A. J., 2013, "Phonon Transport in Periodic Silicon Nanoporous Films With Feature Sizes Greater Than 100 nm," Phys. Rev. B, **87**(19), p. 195301.